




Single-layered phase-change metasurfaces achieving efficient wavefront manipulation and reversible chiral transmission

YIJIA HUANG,^{1,3}  TIANXIAO XIAO,² ZHENGWEI XIE,¹ JIE ZHENG,¹ YARONG SU,¹ WEIDONG CHEN,¹ KE LIU,¹ MINGJUN TANG,¹ JIANQI ZHU,¹ AND LING LI^{1,4}

¹College of Physics and Electronic Engineering, Sichuan Normal University, Chengdu 610101, China

²Physik-Department, Lehrstuhl für Funktionelle Materialien, Technische Universität München, James-Frank-Straße 1, 85748 Garching, Germany

³bradbiubiu@sicnu.edu.cn

⁴lingli70@aliyun.com

Abstract: Efficient control of the phase and polarization of light is of significant importance in modern optics and photonics. However, traditional methods are often accompanied with cascaded and bulky designs that cannot fulfill the ongoing demand for further integrations. Here, a single-layered metasurface composed of nonvolatile phase-change material $\text{Ge}_2\text{Sb}_2\text{Se}_4\text{Te}_1$ (GSST) is proposed with tunable spin-orbit interactions in subwavelength scale. According to the spin-dependent destructive or constructive interference, asymmetric transmission for circularly polarized incidence (extinction ratio $> 8:1$) can be achieved when GSST is in an amorphous state. Moreover, when GSST changes to crystalline state, reversed chiral transmission (extinction ratio $> 12:1$) can be observed due to the existence of intrinsic chirality. In addition, as the average cross-polarized transmitted amplitude is larger than 85%, arbitrary wavefront manipulations can be achieved in both states simultaneously based on the theory of Pancharatnam-Berry phase. As a proof of concept, several functional metasurface devices are designed and characterized to further demonstrate the validation of our design methodology. It is believed that these multifunctional devices with ultrahigh compactness are promising for various applications including chiroptical spectroscopy, EM communication, chiral imaging, and information encryption.

© 2022 Optica Publishing Group under the terms of the [Optica Open Access Publishing Agreement](#)

1. Introduction

Since it was first proposed in 1992, the term ‘spin-orbit interaction (SOI)’ has drawn much attention as it can explain a variety of optical effects, from the spin-Hall effect of light and the spin to vortex conversion to the spin-dependent excitation of surface plasma polaritons and the Pancharatnam–Berry phase [1,2]. It offers a new degree of freedom that the light spin can affect and control the propagation of light and the distribution of the electromagnetic (EM) field. However, although the SOI phenomena are not rare and occur in all basic optical processes, their effects are often negligible since the intrinsic SOI phenomena can only be observed with wavelength scale, which is much smaller than macroscopic length scales for traditional optical systems.

Recent progress of metasurfaces have enabled enriched degree of freedoms to manipulate and control EM waves in terms of amplitude, phase and polarization by introducing strong localized interactions between EM waves and meta atoms [3–5]. Therefore, compared with traditional bulky optical devices such as polarizers and lenses that are unavoidably accompanied with macroscopic thicknesses to accumulate sufficient amplitude or phase differences, metasurfaces with planar geometries and small footprints exhibit great advantages in optics and photonics for miniaturization and integration [6,7]. Moreover, one important feature of metasurfaces is that

they could serve as powerful platforms for the enhancement of SOI, which provide an efficient, scalable, and large bandwidth toolbox for spin-dependent manipulation of light. To date, many exotic phenomena and applications based on SOI in metasurfaces have been realized such as enhanced spin Hall effect [8,9], spin-dependent absorption [10–12], chiral imaging [13,14], optical holograms [15,16], and polarization converters [17,18], to name but a few. However, most previously reported SOI-based metasurfaces were designed with non-tunable single functionality, and the exploration of tunable multifunctional metasurfaces is still in its infancy. As a result, various platforms of reconfigurable metasurfaces based on phase-change materials have been proposed and demonstrated for various promising applications including tunable wavefront control [19–21], reversible optical modulation [22–25], active chirality [26,27] and dynamic color display [28,29].

In this work, we proposed a design methodology for single-layered metasurfaces achieving efficient wavefront manipulation and reversible chiral transmission based on tunable SOI in phase-change material $\text{Ge}_2\text{Sb}_2\text{Se}_4\text{Te}_1$ (hereinafter referred to as GSST). The schematic images are shown in Figs. 1(a) and (b) to conceptually illustrate the performance of the proposed metasurface by tuning the crystallization level of GSST. As shown in Fig. 1(a), when GSST is in amorphous state (A-state), only the right-handed circularly polarized (RCP) EM waves can transmit the metasurface and corresponding encoded information can be obtained in the transmission field, while the EM waves with opposite spin (left-handed circularly polarized, LCP) will be largely blocked. When varying the crystallinity of GSST to crystalline state (C-state) as shown in Fig. 1(b), the chirality of the device is reversed that only the encoded information for the LCP waves can be observed. Compared with previously reported works, the proposed metasurfaces could enable more degrees of freedom for EM wave manipulation since the wavefront and chirality of the incident wave can be controlled simultaneously. Therefore, given the geometrical simplicity and tunable functionality of the proposed metasurfaces, we believe that they could find many integration applications in chiral imaging, chiral sensing, and spin-dependent spectroscopy.

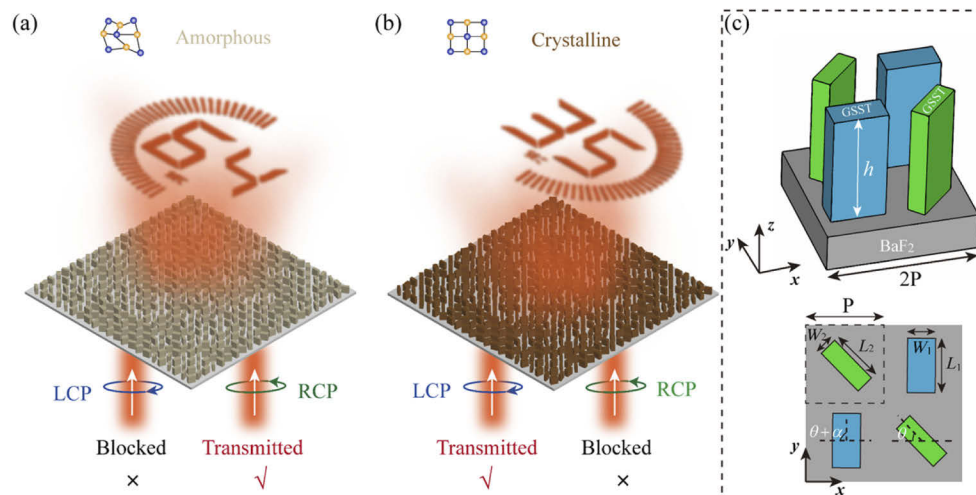


Fig. 1. Schematic images for the proposed single-layered metasurface. (a) When GSST is in A-state, only the RCP EM waves can transmit the metasurface and the corresponding information (“64”) can be observed in the transmission field, while LCP waves are blocked. (b) When GSST changes to C-state, the chirality of the device is reversed and only the information for the LCP waves (“35”) can be observed. (c) 3D (top) and top (bottom) views of the unit cell. The corresponding parameters are $P = 4$, $L_1 = 2.9$, $W_1 = 1.5$, $L_2 = 2.8$, $W_2 = 1$ and $h = 6$ in micrometers.

2. Results and discussions

Figure 1(c) shows the 3D (top) and top (bottom) views of the unit cell for the proposed metasurface that composed of chess-board arranged two pairs of meta atoms labeled with blue and green respectively. The corresponding geometric parameters are given in the figure caption. The material for the unit cell is chosen as GSST for several reasons [30,31]. First, GSST possesses an unprecedented broadband optical transparency with ultralow loss in both A- and C-state in the infrared spectrum, which is an ideal choice for efficient wavefront manipulations [32]. Second, GSST exhibits large optical contrast ($\Delta n = 2.0$) between A- and C-state that could further increase the tunability of the device [30]. Third, as GSST is a nonvolatile material whose crystallization states can be maintained, external stimuli are not needed once GSST is reached at C-state [21]. The permittivities of GSST for the simulations is shown in Appendix A (Fig. 7). The employment of barium fluoride (BaF₂) substrate is due to its low permittivity ($\epsilon=1.96$) that could reduce the reflectance at the bottom surface. In Fig. 1(c), θ is the rotation angle between the main axe of the green meta atom to x -axe and $\alpha=\pi/4$ is the rotation angle difference between adjacent blue and green meta atoms.

The simulated results for the proposed unit cell when GSST is in A-state are shown in Fig. 2. Finite element method in CST Microwave Studio is employed with unit cell boundaries in xy directions and open boundary in z direction. A fine tetrahedral mesh was applied with an adaptive mesh refinement to ensure the accuracy of the results. Figure 2(a) shows the simulated transmittance under RCP and LCP incidence. It can be inferred that the cross-polarized transmittance at 31.4 THz under RCP incidence $T_{RL} = 70\%$ is much larger than other three cases with $T_{RR} = 18\%$, $T_{LL} = 8.5\%$ and $T_{LR} = 2\%$, respectively. Therefore, the total transmittance for RCP and LCP incidence can be calculated as $T_R = T_{RR} + T_{RL} = 88\%$ and $T_L = T_{LL} + T_{LR} = 10.5\%$. Besides, by comparing the normalized electric field distributions in x - z plane under RCP and LCP incidence as shown in Figs. 2(b) and (c), it can be seen that the transmitted field under RCP incidence is much larger than that under LCP incidence that further demonstrates the chiral transmission performance of the unit cell. To further analyze the performance of the unit cell, the total extinction ratio e_{total} and cross-polarized extinction ratio e_{cr} are calculated by

$$e_{total} = \frac{\max(T_R, T_L)}{\min(T_R, T_L)} \quad (1)$$

$$e_{cr} = \frac{\max(T_{RL}, T_{LR})}{\min(T_{RL}, T_{LR})} \quad (2)$$

The calculated results are shown in Fig. 2(d) with $e_{total} = 8.4:1$ and $e_{cr} = 35:1$. Here, the calculation of e_{cr} is to demonstrate that the proposed unit cell can achieve high performance asymmetric wavefront manipulations under circularly polarized incidence since only the cross-polarized components can carry Pancharatnam–Berry phase [33–35]. To investigate the physical mechanism of the chiral transmission, Fig. 2(e) depicts the cross- and co-polarized transmission amplitude for the blue and green meta atoms as a function of frequency. It can be observed that both meta atoms can achieve highly efficient polarization conversion at the working frequency 31.4 THz (denoted by the black dotted line). Besides, the simulated phase for the cross-polarized waves in Fig. 2(f) indicates that the phase difference $\Delta\varphi$ between the meta atoms is close to $\pi/2$ at 31.4 THz. Therefore, the chiral transmission performance of the unit cell in A-state can be explained by the collaborative contributions of SOI (here, the Pancharatnam–Berry phase) and propagation phase [36–39]. To further illustrate this issue, considering the circularly polarized incidence of $[1-i\sigma]^T$ normally illuminates on the meta atoms, the resulting transmitted wave can be written as [40]

$$\cos \frac{\delta}{2} \exp^{i\varphi} \begin{bmatrix} 1 \\ -i\sigma \end{bmatrix} - i \sin \frac{\delta}{2} \exp^{i(-2\sigma\xi+\varphi)} \begin{bmatrix} 1 \\ i\sigma \end{bmatrix} \quad (3)$$

where δ is the phase difference for two orthogonal linear polarizations along the major and minor axes (for a half-wave plate $\delta=\pi$). φ is the polarization-independent propagation phase determined by the size of the meta atom. $-2\sigma\xi$ is the Pancharatnam–Berry phase that $\sigma=\pm 1$ denotes the spin state of circularly polarized incidence and ξ is the rotation angle for the meta atom ($\xi=\theta$ for the green and $\xi=\theta+\alpha$ for the blue meta atoms). Since the polarization conversion ratios for the meta atoms in Fig. 2(a) are sufficiently high, they can be treated as half-wave plates that the first term in Eq (3) can be omitted. Thus, the overall phase difference $\Delta\psi$ in the transmitted field between blue and green meta atoms in the unit cell under the incidence of RCP and LCP waves can be calculated as

$$\Delta\psi = \Delta\varphi + 2\sigma\alpha \quad (4)$$

Since $\Delta\varphi=\pi/2$ and $\alpha=\pi/4$ in this case, the calculated $\Delta\psi$ for $\sigma=1$ (LCP) and -1 (RCP) are π and 0 respectively. According to the interference theory, the LCP incidence experiences destructive interference and being blocked, while the RCP incidence undergoes constructive interference that can transmit through the metasurface and convert to LCP wave carrying Pancharatnam–Berry phase [36].

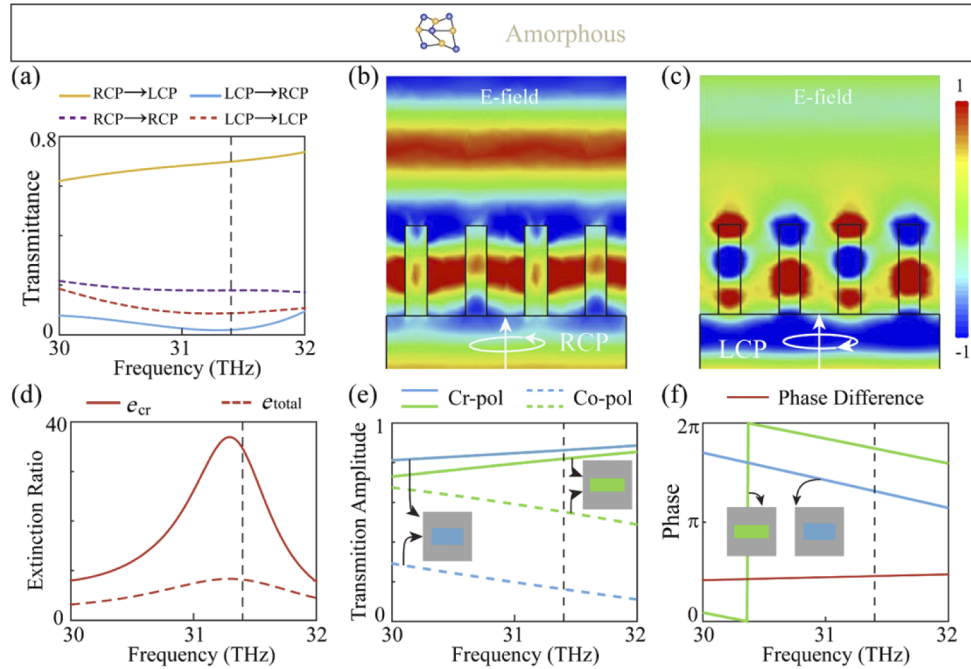


Fig. 2. Simulated results for the proposed unit cell when GSST is in A-state. (a) Simulated transmittance of the unit cell. (b)-(c) Simulated normalized electric field distributions in x - z plane under RCP (b) and LCP (c) incidence. The electric field is normalized to the maximum in (b). (d) Calculated extinction ratio of the unit cell. (e) Simulated transmission amplitude of the meta atoms (f) Simulated transmitted phase for the cross-polarized waves of the meta atoms.

By exploiting the temperature-activated phase transition, for example by hot-plate annealing at 250 °C for 30 min in an ultra-high purity argon atmosphere, the crystallinity of GSST can be varied from A-state to C-state [21,23]. The corresponding performance is shown in Fig. 3. The simulated transmittance of the unit cell under circularly polarized incidence is depicted in Fig. 3(a). In this case, the simulated results at 31.4 THz are $T_{LR} = 66\%$, $T_{LL} = 25\%$, $T_{RR} = 5.4\%$ and $T_{RL} = 2\%$. Therefore, the total transmittance can be calculated as $T_L = 91\%$ and $T_R = 7.4\%$,

which exhibits near perfect transmission and reflection performance for LCP and RCP incidence respectively. The normalized electric field distributions in Figs. 3(b) and (c) further indicate that the chirality is reversed compared with those when GSST is in A-state. The calculated extinction ratios are $e_{\text{total}} = 12.3:1$ and $e_{\text{cr}} = 33:1$ according to Eqs.(1)-(2) as shown in Fig. 3(d). To shed light on corresponding physical mechanism, the transmission amplitude for the green and blue meta atoms are simulated as shown in Figs. 3(a) and (b), respectively. Interestingly, unlike the case in the A-state, the polarization conversion ratios in C-state for both meta atoms are quite low and their phase difference $\Delta\varphi$ largely deviates from $\pi/2$ ($\Delta\varphi \approx \pi/4$), which indicates that the meta atoms do not fulfill the requirement for constructive/destructive interference and thus the chiral transmission performance cannot be explained by interference theory. In fact, akin to previous works [41,42], it is the intrinsic chirality that leads to the asymmetric transmission when GSST is in C-state, since the unit cell with broken rotational symmetries remarkably enhanced the spin-selective performance. One typical feature of intrinsic chirality is that the chiral transmission exhibits multi-resonant characteristics with generally narrow bandwidth. On contrary, the bandwidth for interference-based chiral transmission is broader and without obvious fluctuations as the constructive/destructive interference conditions can be approximately fulfilled in broadband [36–38].

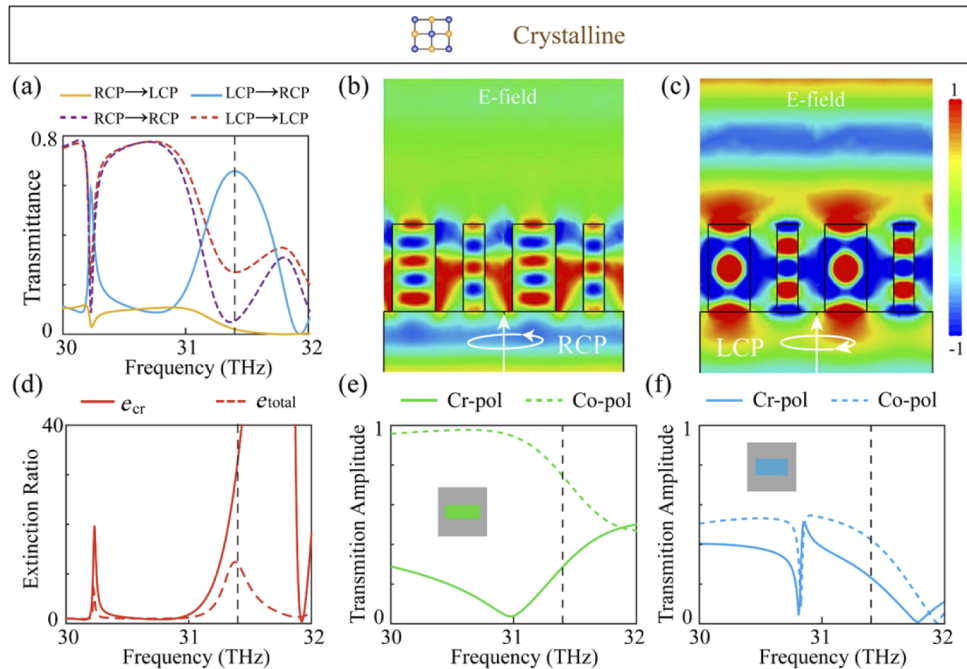


Fig. 3. Simulated results for the proposed unit cell when GSST is in C-state. (a) Simulated transmittance of the unit cell. (b)-(c) Simulated normalized electric field distributions in x - z plane under RCP (b) and LCP (c) incidence. The electric field is normalized to the maximum in (c). (d) Calculated extinction ratio of the unit cell. (e) Simulated transmission amplitude of the green meta atoms. (f) Simulated transmission amplitude of the blue meta atoms.

To further validate the versatility of the proposed design methodology, three types of functional metasurfaces are simulated and characterized. The first functional device based on the proposed chiral unit cell is a beam deflector with corresponding performance shown in Fig. 4. According to the generalized law of refraction [43], the phase distributions under normal incidence can be

calculated by

$$\Delta\zeta = \frac{2\pi f}{c} x \sin(\Phi) \quad (5)$$

where $\Delta\zeta$ is the phase difference between adjacent unit cells, f is the working frequency, x is the spatial location, c is the speed of light and Φ is the deflection angle. Figure 4(a) depicts the ideal and implemented phase distributions for the deflector composed of 16 unit cells (total length = 128 μm) based on Eq.(5). The predesigned deflection angle is $\Phi=15^\circ$ for LCP incidence ($\Phi=-15^\circ$ for RCP incidence according to Pancharatnam–Berry phase). In order to obtain the simulated results of the proposed beam deflector, full-wave simulations were performed using the time domain solver of CST Microwave Studio. Considering the symmetry of the structure, to reduce the amount of calculation, periodic boundaries were employed in y -axis direction and open boundaries were used in x -axis and z -axis direction. The simulated results when GSST is in A-state under RCP and LCP incidence are shown in Figs. 4(b) and (c), respectively. It can be inferred that the incident RCP wave can be efficiently converted to LCP wave and perfectly guided to the predesigned angle $\Phi=-15^\circ$, while only co-polarized wave can be observed under LCP incidence in the transmission field without deflection. The calculated deflection efficiency (defined as the ratio between the deflected intensity to the predesigned angle and incident intensity) for LCP incidence is only 2% compared with that for the RCP incidence. When GSST changes to C-state, the corresponding results are shown in Figs. 4(e) and (f). It can be seen that the incident RCP wave is largely blocked and the LCP incidence can be well deflected to $\Phi=15^\circ$. In this case, the calculated deflection efficiency for LCP incidence is 21 times larger than that for the RCP incidence. Therefore, the above results demonstrate that the designed deflector can achieve efficient wavefront manipulation as well as tunable chiral transmission.

Multi-focus lens has been widely used in imaging systems, detectors, and optical communications [44,45]. The second functional device is a spin-selective multi-focus metalens as shown in Fig. 5. Figure 5(a) depicts the ideal and implemented phase distributions for the metalens composed of 60 unit cells (total length = 480 μm). Considering the implemented phases for opposite spins are reversed based on Pancharatnam–Berry phase, the design process can be concluded as follows. First, since the metalens is designed as a cylindrical lens to reduce the simulation complexity, the phase profiles for RCP and LCP incidence follow

$$\varphi_{RCP} = \frac{2\pi c}{f} [\sqrt{(x - d_{RCP})^2 + F_{RCP}^2} - F_{RCP}] \quad (6)$$

$$\varphi_{LCP} = \frac{2\pi c}{f} [\sqrt{(x - d_{LCP})^2 + F_{LCP}^2} - F_{LCP}] \quad (7)$$

where $d_{RCP}=0$ and $d_{LCP}=120 \mu\text{m}$ are the lateral displacement of the focal points. $F_{RCP}=240 \mu\text{m}$ and $F_{LCP}=320 \mu\text{m}$ are the designed focal lengths. Then, the required phase distribution φ for the multi-focus metalens can be expressed as

$$\varphi = \arg[\exp(-i\varphi_{RCP}) + \exp(i\varphi_{LCP})] \quad (8)$$

The orientation angle θ of the unit cell on the metalens is determined by $\theta=\varphi/2$ according to Pancharatnam–Berry phase. The simulated farfield distributions when GSST is in A- and C-state are given in Figs. 5(b)-(e) with the same simulations setting as above beam deflector. The insets are normalized electric field distributions at $z = F_{RCP}$ (top) and $z = F_{LCP}$ (bottom). Appendix B (Fig. 8) depicts corresponding theoretical results for comparison. Obviously, the simulated results agreed well with the theoretical counterparts that only RCP (LCP) incidence can be focused to predesigned focus when GSST is in A- (C-) state, while the opposite spin will be blocked. Therefore, the focus of the metalens can be adjusted according to the incident spin states by changing the crystallinity of GSST, which is beneficial for chiral sensing and imaging.

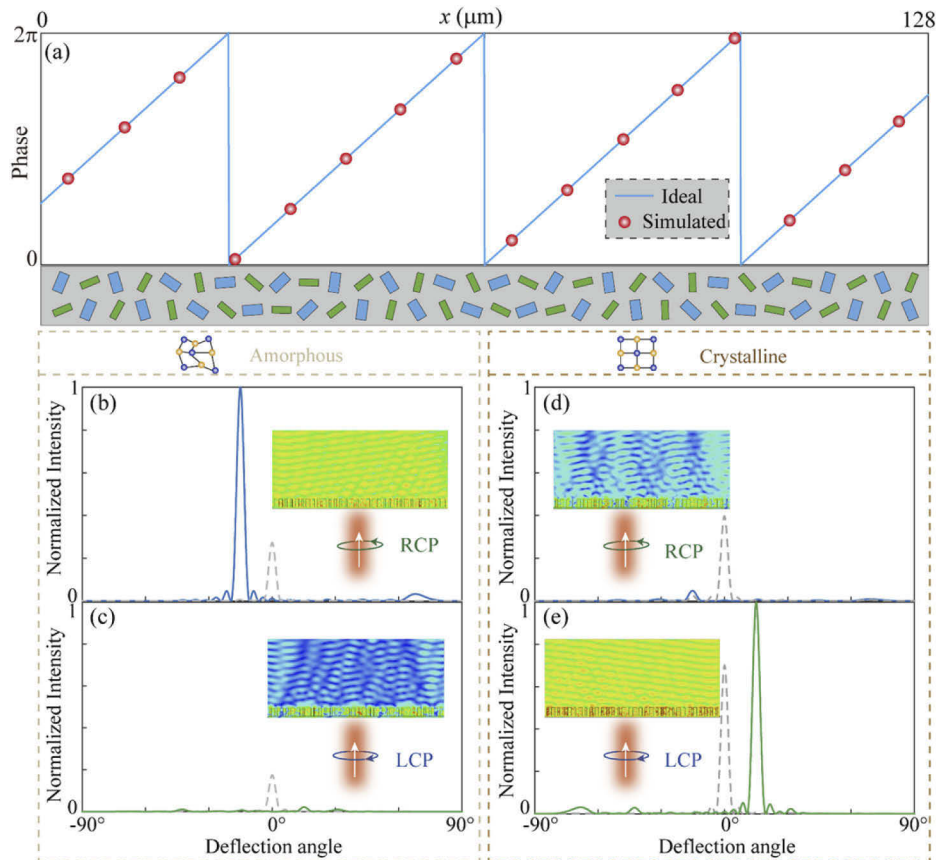


Fig. 4. Spin-selective beam deflector. (a) Ideal (solid line) and simulated (dot) phase distributions for the deflector. (b)-(c) Normalized deflection patterns under RCP (b) and LCP (c) incidence when GSST is in A-state. The intensity is normalized to the maximum in (b). (d)-(e) Normalized deflection patterns under RCP (d) and LCP (e) incidence when GSST is in C-state. The intensity is normalized to the maximum in (e). The insets in (b)-(e) are corresponding normalized electric field distributions. The solid lines correspond to cross polarized wave and dotted lines denote the co-polarized wave.

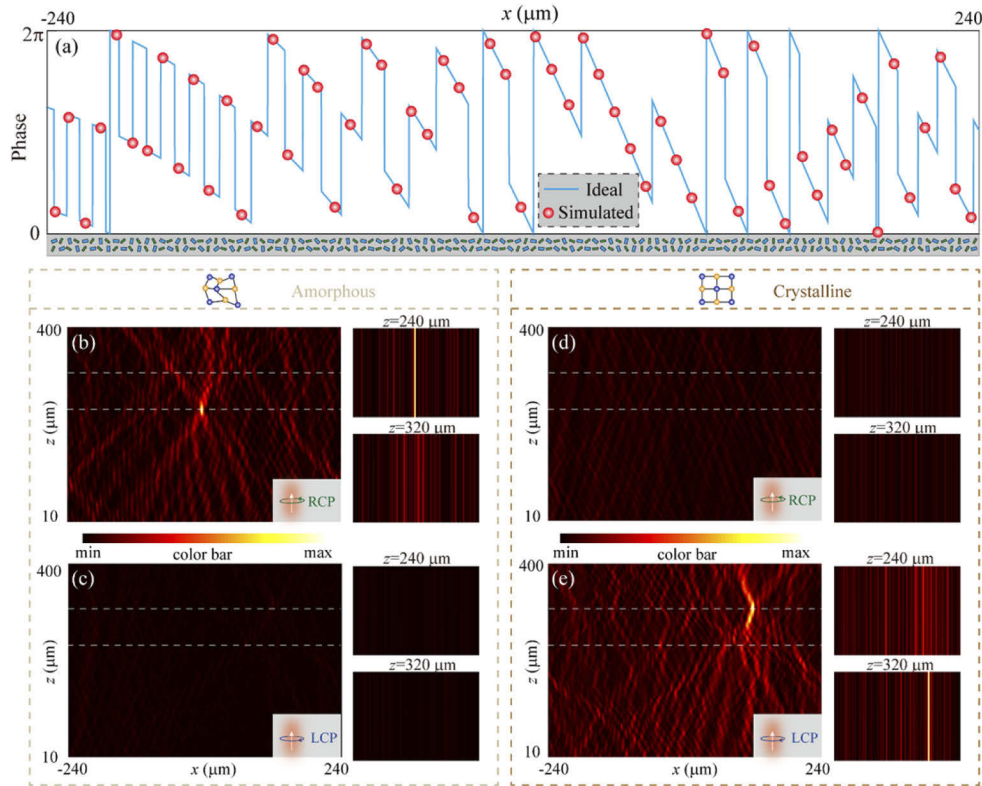


Fig. 5. Spin-selective multi-focus metasurfaces. (a) Ideal (solid line) and simulated (dot) phase distributions for the metasurfaces. (b)-(c) Normalized farfield distributions under RCP (b) and LCP (c) incidence when GSST is in A-state. The intensity is normalized to the maximum in (b). (d)-(e) Normalized farfield distributions under RCP (d) and LCP (e) incidence when GSST is in C-state. The intensity is normalized to the maximum in (e). The insets in (b)-(e) are corresponding normalized electric field distributions at $z = F_{RCP}$ and $z = F_{LCP}$.

Moreover, simultaneous asymmetric transmission and wavefront manipulation provided by the proposed metasurface can be applied in a wide variety of applications associated with information encryption [46,47]. As a proof of concept, the third functional device is a metasurface for chiral holograms with 1000×1000 unit cells. The target images for RCP (left panel) and LCP (right panel) incidence are shown in Figs. 6(a). The distance between the image plane and metasurface is set as 1.2 mm. Point source algorithm is adapted to obtain the phase distributions φ_{RCP} (left panel in Fig. 6(b)) and φ_{LCP} (middle panel in Fig. 6(b)) [48]. Then the phase distributions (right panel in Fig. 6(b)) for the metasurface is obtained based on Eq. (8). Vectorial diffraction theory is used to calculate the normalized farfield distributions in Figs. 6(c)-(h) [49]. The phase and amplitude at each position on the metasurface is retrieved from corresponding simulated results in Figs. 2(a) and 3(a) according to the incident polarization. Figures 6(c)-(e) depict the calculated results under different polarized incidence when GSST is in A-state. It can be inferred that only the predesigned information for RCP incidence can be well obtained, while the information for LCP incidence is perfectly hidden. In this case, the information channel is “ON” for the RCP wave and “OFF” for the LCP wave. When GSST changes to C-state, the holographic image under RCP incidence cannot be observed as shown in Fig. 6(f), which indicates that the information channel for RCP is switched to “OFF” state. Meanwhile, the previously encrypted information for LCP incidence can be obtained. The results under unpolarized incidence in Figs. 6(e) and (h)

further demonstrate that the information encryption performance of the proposed metasurface can be achieved regardless of the incident polarizations.

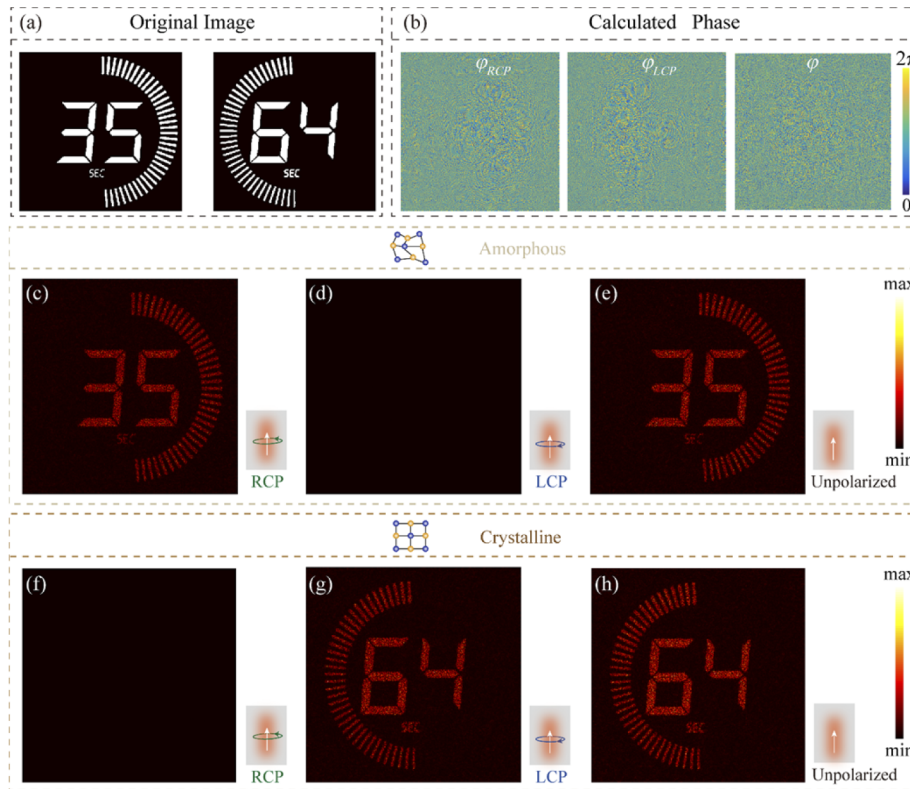


Fig. 6. Chiral holograms for information encryption. (a) Original images for RCP (left) and LCP (right) incidence. (b) Calculated phase distributions. (c)-(e) Normalized farfield distributions under RCP (c), LCP (d) and unpolarized (e) incidence when GSST is in A-state. The intensity is normalized to the maximum in (c). (f)-(h) Normalized farfield distributions under RCP (f), LCP (g) and unpolarized (h) incidence when GSST is in C-state. The intensity is normalized to the maximum in (g).

3. Conclusion

Although subsequent experiments are not performed in the presented work, many previously reported works have been demonstrated that the fabrication of structured phase-change meta atoms with high aspect ratio can be achieved by the state-of-art nanofabrication technologies [21,50,51]. Besides, the reamorphize of GSST meta atoms with thickness up to several micrometers is still an open question in this field that fully reamorphization of the proposed devices may not be achievable at present. However, this problem may be solved by several methods. For example, by applying the design principle at higher frequencies according to scalability of Maxwell's equations, the thickness of GSST can be further reduced to meet the requirement for reamorphization. Additionally, recent works have demonstrated that the reamorphization of GSST and other phase-change materials can be achieved by varies methods. The achieved reamorphization thickness increased from initial tens of nanometers to current hundreds of nanometers [23,29,52,53]. Since the theoretical reversible thickness of GSST film can approach

several micrometers [21], the reamorphization of the proposed devices may be achievable in the near future.

In summary, a generalized design methodology for spin-selective metasurfaces is proposed in this paper. By exploiting the phase transition of GSST to introduce tunable SOI, a single-layered metasurface can achieve efficient wavefront manipulation and reversible chiral transmission simultaneously. The inner physics is further explained by interference theory and intrinsic chirality. The chiral transmission performance of the proposed metasurface in both A- (8.4:1) and C-state (12.3:1) is comparable and even better than previously reported works as shown in Appendix C. Besides, simulated results validate that the proposed chiral metasurface can be applied to spin- and temperature-coded information encryption, i.e., multiple channels of information can be coded with enriched freedoms. Considering the nearly dispersionless permittivity of GSST throughout almost the entire infrared spectrum, the design principle can be further employed for other frequencies, which will enable more fascinating applications in optics and photonics, such as polarimetry, chiral sensing and imaging.

APPENDIX A: Permittivity of GSST

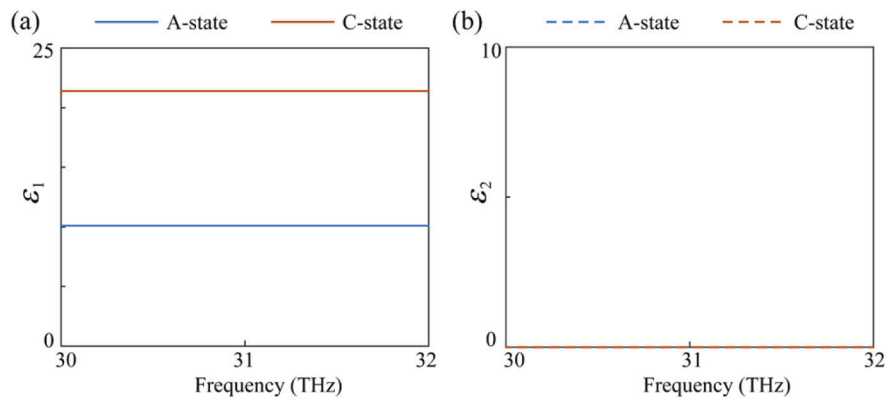


Fig. 7. (a) Real part of permittivities ϵ_1 when GSST is in A- and C-state. (b) Imaginary part of permittivities ϵ_2 when GSST is in A- and C-state. The permittivities are obtained from measured results in ref [30].

APPENDIX B: Theoretical results for the designed metalens

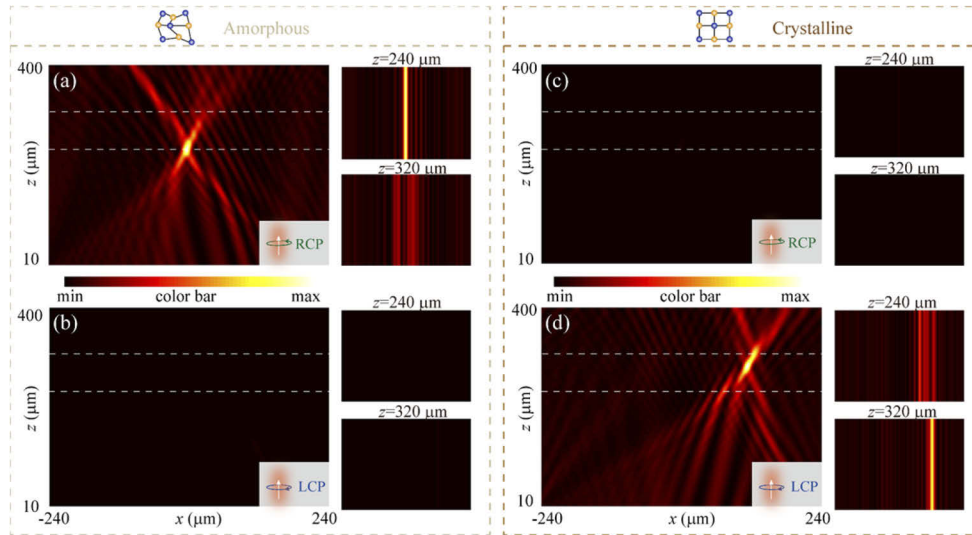


Fig. 8. (a)-(b) Normalized farfield distributions under RCP (a) and LCP (b) incidence when GSST is in A-state. The intensity is normalized to the maximum in (a). (c)-(d) Normalized farfield distributions under RCP (c) and LCP (d) incidence when GSST is in C-state. The intensity is normalized to the maximum in (d). The insets in (b)-(e) are corresponding normalized electric field distributions at $z = F_{RCP}$ and $z = F_{LCP}$. The theoretical results are calculated by vectorial diffraction theory. The phase and amplitude at each position on the metalems is retrieved from corresponding simulated results in Figs. 2(a) and 3(a) according to the incident polarization.

APPENDIX C: Comparison with reported chiral transmission metasurfaces

	Extinction ratio	Wavefront manipulation
Ref [36]	$\approx 17:1$ in simulation $\approx 10:1$ in experiment	Yes
Ref [37]	$\approx 4.5:1$ in simulation $\approx 3.5:1$ in experiment	No
Ref [38]	$\approx 3.5:1$ in simulation $\approx 3:1$ in experiment	Yes
Ref [42]	$\approx 17:1$ in simulation $\approx 10:1$ in experiment	No
Our work	8.4:1 when GSST in A-state 12.3:1 when GSST in C-state	Yes

Funding. Opening Foundation of State Key Laboratory of Optical Technologies on Nano-Fabrication and Micro-Engineering; National Natural Science Foundation of China (12104326, 12104329, 62105228).

Disclosures. The authors declare no conflicts of interest.

Data availability. Data underlying the results presented in this paper are not publicly available at this time but may be obtained from the authors upon reasonable request.

References

1. K. Y. Bliokh, F. J. Rodríguez-Fortuño, F. Nori, and A. V. Zayats, "Spin-orbit interactions of light," *Nat. Photonics* **9**(12), 796–808 (2015).
2. F. Cardano and L. Marrucci, "Spin-orbit photonics," *Nat. Photonics* **9**(12), 776–778 (2015).
3. N. Yu and F. Capasso, "Flat optics with designer metasurfaces," *Nat. Mater.* **13**(2), 139 (2014).
4. W. T. Chen, A. Y. Zhu, and F. Capasso, "Flat optics with dispersion-engineered metasurfaces," *Nat. Rev. Mater.* **5**(8), 604–620 (2020).
5. X. Luo, D. Tsai, M. Gu, and M. Hong, "Extraordinary optical fields in nanostructures: from sub-diffraction-limited optics to sensing and energy conversion," *Chem. Soc. Rev.* **48**(8), 2458–2494 (2019).
6. X. Luo, "Engineering Optics 2.0: A Revolution in Optical Materials, Devices, and Systems," *ACS Photonics* **5**(12), 4724–4738 (2018).
7. X. Luo, "Subwavelength Artificial Structures: Opening a New Era for Engineering Optics," *Adv. Mater.* **31**(4), 1804680 (2019).
8. X. Yin, Z. Ye, J. Rho, Y. Wang, and X. Zhang, "Photonic Spin Hall Effect at Metasurfaces," *Science* **339**(6126), 1405–1407 (2013).
9. X.-G. Luo, M.-B. Pu, X. Li, and X.-L. Ma, "Broadband spin Hall effect of light in single nanoapertures," *Light Sci Appl* **6**(6), e16276 (2017).
10. J. Qin, L. Deng, T. Kang, L. Nie, H. Feng, H. Wang, R. Yang, X. Liang, T. Tang, J. Shen, C. Li, H. Wang, Y. Luo, G. Armelles, and L. Bi, "Switching the Optical Chirality in Magnetoplasmonic Metasurfaces Using Applied Magnetic Fields," *ACS Nano* **14**(3), 2808–2816 (2020).
11. E. Plum and N. I. Zheludev, "Chiral mirrors," *Appl. Phys. Lett.* **106**(22), 221901 (2015).
12. Y. Huang, T. Xiao, Z. Xie, J. Zheng, Y. Su, W. Chen, K. Liu, M. Tang, P. Müller-Buschbaum, and L. Li, "Single-Layered Reflective Metasurface Achieving Simultaneous Spin-Selective Perfect Absorption and Efficient Wavefront Manipulation," *Adv. Opt. Mater.* **9**(5), 2001663 (2021).
13. P. Huo, C. Zhang, W. Zhu, M. Liu, S. Zhang, S. Zhang, L. Chen, H. J. Lezec, A. Agrawal, Y. Lu, and T. Xu, "Photonic Spin-Multiplexing Metasurface for Switchable Spiral Phase Contrast Imaging," *Nano Lett.* **20**(4), 2791–2798 (2020).
14. M. Khorasaninejad, W. T. Chen, A. Y. Zhu, J. Oh, R. C. Devlin, D. Rousso, and F. Capasso, "Multispectral Chiral Imaging with a Metalens," *Nano Lett.* **16**(7), 4595–4600 (2016).
15. X. Zhang, M. Pu, Y. Guo, J. Jin, X. Li, X. Ma, J. Luo, C. Wang, and X. Luo, "Colorful Metahologram with Independently Controlled Images in Transmission and Reflection Spaces," *Adv. Funct. Mater.* **29**(22), 1809145 (2019).
16. Z.-L. Deng, M. Jin, X. Ye, S. Wang, T. Shi, J. Deng, N. Mao, Y. Cao, B.-O. Guan, A. Alù, G. Li, and X. Li, "Full-Color Complex-Amplitude Vectorial Holograms Based on Multi-Freedom Metasurfaces," *Adv. Funct. Mater.* **30**(21), 1910610 (2020).
17. X. Ma, M. Pu, X. Li, Y. Guo, and X. Luo, "All-metallic wide-angle metasurfaces for multifunctional polarization manipulation," *Opto-Electron. Adv.* **2**(3), 1800231 (2019).
18. Q. Lévesque, M. Makhisyian, P. Bouchon, F. Pardo, J. Jaeck, N. Bardou, C. Dupuis, R. Haïdar, and J.-L. Pelouard, "Plasmonic planar antenna for wideband and efficient linear polarization conversion," *Appl. Phys. Lett.* **104**(11), 111105 (2014).
19. F. Zhang, X. Xie, M. Pu, Y. Guo, X. Ma, X. Li, J. Luo, Q. He, H. Yu, and X. Luo, "Multistate Switching of Photonic Angular Momentum Coupling in Phase-Change Metadevices," *Adv. Mater.* **32**(39), 1908194 (2020).
20. M. Zhang, M. Pu, F. Zhang, Y. Guo, Q. He, X. Ma, Y. Huang, X. Li, H. Yu, and X. Luo, "Plasmonic Metasurfaces for Switchable Photonic Spin-Orbit Interactions Based on Phase Change Materials," *Adv. Sci.* **5**(10), 1800835 (2018).
21. M. Y. Shalaginov, S. An, Y. Zhang, F. Yang, P. Su, V. Liberman, J. B. Chou, C. M. Roberts, M. Kang, and C. Rios, "Reconfigurable all-dielectric metalens with diffraction-limited performance," *Nat. Commun.* **12**(1), 1225 (2021).
22. S. Abdollahramezani, O. Hemmatyar, M. Taghinejad, H. Taghinejad, A. Krasnok, A. A. Eftekhar, C. Teichrib, S. Deshmukh, M. El-Sayed, E. Pop, M. Wuttig, A. Alu, W. Cai, and A. Adibi, "Electrically driven programmable phase-change meta-switch reaching 80% efficiency," *ArXiv E-Prints arXiv:2104.10381* (2021).
23. Y. Zhang, C. Fowler, J. Liang, B. Azhar, M. Y. Shalaginov, S. Deckoff-Jones, S. An, J. B. Chou, C. M. Roberts, and V. Liberman, "Electrically reconfigurable non-volatile metasurface using low-loss optical phase-change material," *Nat. Nanotechnol.* **16**(6), 661–666 (2021).
24. Y. Wang, P. Landreman, D. Schoen, K. Okabe, A. Marshall, U. Celano, H.-S. P. Wong, J. Park, and M. L. Brongersma, "Electrical tuning of phase-change antennas and metasurfaces," *Nat. Nanotechnol.* **16**(6), 667–672 (2021).
25. S. Abdollahramezani, O. Hemmatyar, M. Taghinejad, H. Taghinejad, Y. Kiarashinejad, M. Zandehshahvar, T. Fan, S. Deshmukh, A. A. Eftekhar, W. Cai, E. Pop, M. A. El-Sayed, and A. Adibi, "Dynamic Hybrid Metasurfaces," *Nano Lett.* **21**(3), 1238–1245 (2021).
26. X. Yin, M. Schäferling, A.-K. U. Michel, A. Tittl, M. Wuttig, T. Taubner, and H. Giessen, "Active Chiral Plasmonics," *Nano Lett.* **15**(7), 4255–4260 (2015).
27. Y. Huang, T. Xiao, Z. Xie, J. Zheng, Y. Su, W. Chen, K. Liu, M. Tang, J. Zhu, P. Müller-Buschbaum, and L. Li, "Multistate Nonvolatile Metamirrors with Tunable Optical Chirality," *ACS Appl. Mater. Interfaces* **13**(38), 45890–45897 (2021).

28. S. G.-C. Carrillo, L. Trimby, Y.-Y. Au, V. K. Nagareddy, G. Rodriguez-Hernandez, P. Hosseini, C. Ríos, H. Bhaskaran, and C. D. Wright, "A Nonvolatile Phase-Change Metamaterial Color Display," *Adv. Opt. Mater.* **7**(18), 1801782 (2019).
29. O. Hemmatyar, S. Abdollahramezani, I. Zeimpekis, S. Lepeshov, A. Krasnok, A. Intisar Khan, K. M. Neilson, C. Teichrib, T. Brown, E. Pop, D. W. Hewak, M. Wuttig, A. Alu, O. L. Muskens, and A. Adibi, "Enhanced Meta-Displays Using Advanced Phase-Change Materials," ArXiv E-Prints arXiv:2107.12159 (2021).
30. Y. Zhang, J. B. Chou, J. Li, H. Li, Q. Du, A. Yadav, S. Zhou, M. Y. Shalaginov, Z. Fang, H. Zhong, C. Roberts, P. Robinson, B. Bohlin, C. Ríos, H. Lin, M. Kang, T. Gu, J. Warner, V. Liberman, K. Richardson, and J. Hu, "Broadband transparent optical phase change materials for high-performance nonvolatile photonics," *Nat. Commun.* **10**(1), 4279 (2019).
31. M. Wuttig, H. Bhaskaran, and T. Taubner, "Phase-change materials for non-volatile photonic applications," *Nat. Photonics* **11**(8), 465–476 (2017).
32. C. Zhou, Z. Xie, B. Zhang, T. Lei, Z. Li, L. Du, and X. Yuan, "Reconfigurable dielectric metasurface for active wavefront modulation based on a phase-change material metamolecule design," *Opt. Express* **28**(25), 38241–38251 (2020).
33. Xin Xie, Kaipeng Liu, Mingbo Pu, Xiaoliang Ma, Xiong Li, Yinghui Guo, Fei Zhang, and Xiangang Luo, "All-metallic geometric metasurfaces for broadband and high-efficiency wavefront manipulation," *Nanophotonics* **9**(10), 3209–3215 (2020).
34. G. Yoon, D. Lee, K. T. Nam, and J. Rho, "Geometric metasurface enabling polarization independent beam splitting," *Sci. Rep.* **8**(1), 9468 (2018).
35. E. Hasman, V. Kleiner, G. Biener, and A. Niv, "Polarization dependent focusing lens by use of quantized Pancharatnam–Berry phase diffractive optics," *Appl. Phys. Lett.* **82**(3), 328–330 (2003).
36. F. Zhang, M. Pu, X. Li, P. Gao, X. Ma, J. Luo, H. Yu, and X. Luo, "All-Dielectric Metasurfaces for Simultaneous Giant Circular Asymmetric Transmission and Wavefront Shaping Based on Asymmetric Photonic Spin–Orbit Interactions," *Adv. Funct. Mater.* **27**(47), 1704295 (2017).
37. M. Kenney, S. Li, X. Zhang, X. Su, T.-T. Kim, D. Wang, D. Wu, C. Ouyang, J. Han, W. Zhang, H. Sun, and S. Zhang, "Pancharatnam–Berry Phase Induced Spin-Selective Transmission in Herringbone Dielectric Metamaterials," *Adv. Mater.* **28**(43), 9567–9572 (2016).
38. C. Zheng, J. Li, J. Li, Z. Yue, S. Wang, M. Li, H. Zhao, X. Hao, H. Zang, Y. Zhang, and J. Yao, "All-silicon chiral metasurfaces and wavefront shaping assisted by interference," *Sci. China Phys. Mech. Astron.* **64**(11), 114212 (2021).
39. M. Liu, P. Huo, W. Zhu, C. Zhang, S. Zhang, M. Song, S. Zhang, Q. Zhou, L. Chen, H. J. Lezec, A. Agrawal, Y. Lu, and T. Xu, "Broadband generation of perfect Poincaré beams via dielectric spin-multiplexed metasurface," *Nat. Commun.* **12**(1), 2230 (2021).
40. J. P. Balthasar Mueller, N. A. Rubin, R. C. Devlin, B. Groever, and F. Capasso, "Metasurface Polarization Optics: Independent Phase Control of Arbitrary Orthogonal States of Polarization," *Phys. Rev. Lett.* **118**(11), 113901 (2017).
41. C. Wu, N. Arju, G. Kelp, J. A. Fan, J. Dominguez, E. Gonzales, E. Tutuc, I. Brener, and G. Shvets, "Spectrally selective chiral silicon metasurfaces based on infrared Fano resonances," *Nat. Commun.* **5**(1), 3892 (2014).
42. A. Y. Zhu, W. T. Chen, A. Zaidi, Y.-W. Huang, M. Khorasaninejad, V. Sanjeev, C.-W. Qiu, and F. Capasso, "Giant intrinsic chiro-optical activity in planar dielectric nanostructures," *Light Sci Appl* **7**(2), 17158 (2018).
43. N. Yu, P. Genevet, M. A. Kats, F. Aieta, J.-P. Tetienne, F. Capasso, and Z. Gaburro, "Light Propagation with Phase Discontinuities: Generalized Laws of Reflection and Refraction," *Science* **334**(6054), 333–337 (2011).
44. G. D. Bai, Q. Ma, S. Iqbal, L. Bao, H. B. Jing, L. Zhang, H. T. Wu, R. Y. Wu, H. C. Zhang, C. Yang, and T. J. Cui, "Multitasking Shared Aperture Enabled with Multiband Digital Coding Metasurface," *Adv. Opt. Mater.* **6**(21), 1800657 (2018).
45. Jinying Guo, Teng Wang, Baogang Quan, Huan Zhao, Changzhi Gu, Junjie Li, Xinke Wang, Guohai Situ, and Yan Zhang, "Polarization multiplexing for double images display," *Opto-Electron. Adv.* **2**(7), 180029 (2019).
46. H. Gao, X. Fan, W. Xiong, and M. Hong, "Recent advances in optical dynamic meta-holography," *Opto-Electron. Adv.* **4**(11), 2100301 (2021).
47. Arash Nemati, Qian Wang, Minghui Hong, and Jinghua Teng, "Tunable and reconfigurable metasurfaces and metadevices," *Opto-Electron. Adv.* **1**(5), 180009 (2018).
48. X. Li, L. Chen, Y. Li, X. Zhang, M. Pu, Z. Zhao, X. Ma, Y. Wang, M. Hong, and X. Luo, "Multicolor 3D meta-holography by broadband plasmonic modulation," *Sci. Adv.* **2**(11), e1601102 (2016).
49. M. Pu, X. Li, X. Ma, Y. Wang, Z. Zhao, C. Wang, C. Hu, P. Gao, C. Huang, H. Ren, X. Li, F. Qin, J. Yang, M. Gu, M. Hong, and X. Luo, "Catenary optics for achromatic generation of perfect optical angular momentum," *Sci. Adv.* **1**(9), e1500396 (2015).
50. S. Abdollahramezani, O. Hemmatyar, H. Taghinejad, A. Krasnok, Y. Kiarashinejad, M. Zandehshahvar, A. Alù, and A. Adibi, "Tunable nanophotonics enabled by chalcogenide phase-change materials," *Nanophotonics* **9**(5), 1189–1241 (2020).
51. C. Choi, S.-Y. Lee, S.-E. Mun, G.-Y. Lee, J. Sung, H. Yun, J.-H. Yang, H.-O. Kim, C.-Y. Hwang, and B. Lee, "Metasurface with Nanostructured Ge₂Sb₂Te₅ as a Platform for Broadband-Operating Wavefront Switch," *Adv. Opt. Mater.* **7**(12), 1900171 (2019).

52. A.-K. U. Michel, P. Zalden, D. N. Chigrin, M. Wuttig, A. M. Lindenberg, and T. Taubner, "Reversible Optical Switching of Infrared Antenna Resonances with Ultrathin Phase-Change Layers Using Femtosecond Laser Pulses," *ACS Photonics* **1**(9), 833–839 (2014).
53. O. Hemmatyar, S. Abdollahramezani, H. Taghinejad, and A. Adibi, "Electrically tunable phase-change metasurfaces using transparent conductive oxide microheaters," in *Conference on Lasers and Electro-Optics*, J. Kang Tomasulo, S. Ilev, I. Müller, D. Litchinitser, N. Polyakov, S. Podolskiy, V. Nunn, J. Dorrer, C. Fortier, T. Gan, Q. , and C. Saraceno (eds.), OSA Technical Digest (Optical Society of America, 2021), p. FTh4 K.1.